JGR Atmospheres

RESEARCH ARTICLE
10.1029/2022JD038011

Atmospheric Climatologies Over Isfjorden, Svalbard

L. Frank[1,2], M. O. Jonassen[1,2], R. Skogseth[1], and T. Vihma[1,3]

[1]Department of Arctic Geophysics, The University Centre in Svalbard, Longyearbyen, Norway, [2]Geophysical Institute, University of Bergen, Bergen, Norway, [3]Finnish Meteorological Institute, Helsinki, Finland

Key Points:

- Climatologies of near-surface variables over Isfjorden are strongly impacted by the land-sea contrast and orography
- Temporal variability dominates over spatial variability, but both depend on the season and the synoptic-scale flow

Supporting Information:

Supporting Information may be found in the online version of this article.

Correspondence to:

L. Frank,
lukasf@unis.no

Citation:

Frank, L., Jonassen, M. O., Skogseth, R., & Vihma, T. (2023). Atmospheric climatologies over Isfjorden, Svalbard. *Journal of Geophysical Research: Atmospheres*, *128*, e2022JD038011. https://doi.org/10.1029/2022JD038011

Received 12 OCT 2022
Accepted 24 OCT 2023

Author Contributions:

Formal analysis: L. Frank
Investigation: L. Frank
Methodology: L. Frank
Project Administration: M. O. Jonassen
Supervision: M. O. Jonassen, R. Skogseth, T. Vihma
Visualization: L. Frank
Writing – original draft: L. Frank
Writing – review & editing: L. Frank

Abstract The Isfjorden region at the west coast of Spitsbergen is the most easily accessible area in the Svalbard Archipelago, making it a perfect outdoor laboratory for Arctic research. Due to its location in the high Arctic together with its complex terrain, the climatic conditions vary substantially both in time and space. Based on a new high-resolution reanalysis, we present climatologies of five major atmospheric variables over the Isfjorden region during 2011–2021 with special focus on local effects. For example, we find that topographic channeling effects often lead to differences in near-surface wind speeds of several m s^{-1} over small horizontal distances. During winter, the fjord acts as a heat and moisture island, ultimately impacting the adjacent low-elevation land areas. These land–sea gradients reverse during summer. High mountain areas surrounding the fjord experience substantially different climatic conditions, with for example, seasonal precipitation doubling from sea level to approximately 700 m. The spatial variability over the Isfjorden region is in general found to be smaller than its temporal counterpart but larger than the diurnal cycle. Besides these findings, this study furthermore demonstrates the importance of high-resolution regional atmospheric reanalyses compared to global products for the characterization of the local micro-climate over Arctic fjords and the interaction with surrounding land areas.

Plain Language Summary The Isfjorden region at the west coast of Spitsbergen is the most easily accessible area in the Svalbard Archipelago, making it a perfect outdoor laboratory for Arctic research. Due to its location in the high Arctic together with its complex terrain, the climatic conditions vary substantially both in time and space. In this study, we use high resolution model data to present climatologies of five major meteorological variables during 2011–2021. We focus on the Isfjorden region in central Svalbard, which is the most populated area in the archipelago. Our results reveal that winds get strongly enhanced locally through channeling along valleys and fjords, and can vary by several m s^{-1} over small horizontal distances. During winter, the warm water in Isfjorden (relative to the cold air aloft) heats the near-surface atmosphere above the adjacent land areas. Precipitation doubles from sea level to approximately 700 m. Besides these findings, we argue that model products with high resolution are highly useful tools for investigating the local micro-climate in Arctic fjord systems with complex topography such as Isfjorden.

1. Introduction

The Svalbard Archipelago in the high European Arctic is located at 74°–81°N, 10°–35°E. Due to this location at the eastern rim of the Fram Strait, the climatic conditions are much less extreme than in other regions at the same latitudes. Extratropical-latitude cyclones traveling northwards along the North Atlantic storm track periodically transport warm and moist air into the regions around Svalbard (Wickström, Jonassen, Vihma, & Uotila, 2020; Zahn et al., 2018). In the ocean, the West Spitsbergen Current (WSC) flowing northwards in eastern Fram Strait releases heat to the atmosphere, especially during winter (Boyd & D'Asaro, 1994; Carmack et al., 2015), and strongly impacts the climate and sea ice conditions along the west coast of Spitsbergen and its fjords (Cottier et al., 2007; Muckenhuber et al., 2016; Nilsen et al., 2016; Skogseth et al., 2020; Tverberg et al., 2019; Walczowski & Piechura, 2011).

However, the local weather conditions in Svalbard do not only strongly depend on the synoptic situation. The complex topography and the large variations in the surface temperature, specific humidity and aerodynamic roughness lead to phenomena like channeling effects (e.g., Kossmann & Sturman, 2003; Skeie & Gronas, 2000; Whiteman & Doran, 1993), gap winds (Jackson & Steyn, 1994), tip jets (Reeve & Kolstad, 2011), coastal jets (Furevik et al., 2002; Sandvik & Furevik, 2002) or low-level jets (Vihma et al., 2011) in the wind fields. Fjords extending up to 100 km inland provide large heat and moisture reservoirs for the atmosphere, leading to the formation of heat islands and associated small-scale circulations like land-sea-breezes (Esau & Repina, 2012).

In the currently observed climate change, the Arctic has been warming up to four times faster than the global average (Rantanen et al., 2022; Serreze & Barry, 2011; Smith et al., 2019), and Svalbard is in the hot spot of this warming (e.g., Hanssen-Bauer et al., 2019). The weaker meridional temperature gradient between mid and high latitudes favors larger Rossby wave meandering (Screen & Simmonds, 2013). The North Atlantic storm track adjusts to the resulting enhanced meridional circulation patterns (Zahn et al., 2018), so that a significant increase in winter cyclone activity has been seen around Svalbard, while more zonal cyclone paths into the southeastern Barents Sea are less frequent (Wickström, Jonassen, Vihma, & Uotila, 2020). In addition, the strong loss of sea ice north (Onarheim et al., 2014) and east (Smedsrud et al., 2013) of Svalbard exposes the cold atmosphere to the relatively warm ocean, which during wintertime is a large source for atmospheric heat and moisture (Smedsrud et al., 2010).

Several studies have already addressed the local climatic conditions and the imprint of climate change in the atmosphere over Svalbard. Interest has been focused on the temperature increase (e.g., Førland et al., 1997; Førland et al., 2011; Gjelten et al., 2016; Isaksen et al., 2016; Isaksen et al., 2022; Nordli et al., 2014), the sea ice retreat in the fjords (e.g., Dahlke et al., 2020; Muckenhuber et al., 2016) and extreme weather events of precipitation and rain-on-snow (Peeters et al., 2019; Wickström, Jonassen, Cassano, & Vihma, 2020), due to their hazard potential for the local community as well as shipping, tourism and basically any other human activity in the region.

Studies mostly relying on observational time series might utilize the most realistic data available for the respective locations, but in turn lack spatial representativeness for larger areas and are furthermore biased toward measurements over land surfaces. Numerical weather prediction (NWP) and climate model data can overcome these limitations, but have so far been too coarse to adequately resolve the complex topography and variable surface properties of Svalbard (e.g., the global reanalysis ERA5, horizontal resolution 31 km, Hersbach et al. (2020)). Furthermore, conditions typical for the Arctic such as stable (atmospheric) boundary layers (Køltzow et al., 2019; Zilitinkevich & Esau, 2005), air-ice-sea interaction processes and the sparse observational network are challenging for NWP systems and cause further uncertainties (Vihma et al., 2014).

Only recently, advances in numerical modeling and parameterizations have led to substantial improvement of model representations for the Arctic (Bromwich et al., 2016), although not much with respect to the stable boundary layer (Haiden et al., 2018; Køltzow et al., 2019). At the Norwegian Meteorological Institute (MET Norway), the AROME-Arctic NWP model has been run operationally since 2015 with a horizontal resolution of 2.5 km, covering large parts of Fennoscandia and the European Arctic, including Svalbard (Müller et al., 2017). It has shown to perform well compared to for example, the global forecasting model of the European Centre of Medium-Range Weather Forecasting (ECMWF) (Køltzow et al., 2019). Based on these experiences and addressing the need for high-resolution model representations of the Arctic atmosphere over complex terrain, the Copernicus Arctic Regional Reanalysis (CARRA) was developed. In a first evaluation of basic atmospheric variables, Køltzow et al. (2022) find that CARRA outperforms ERA5 when compared against observations, including MET Norway's stations in the Isfjorden region (Svalbard Airport and Isfjord Radio). Moore and Imrit (2022) furthermore show that in contrast to ERA5, CARRA adequately represents the atmospheric near-surface wind fields in a narrow ocean strait with characteristics similar to Isfjorden in terms of its width and surrounding topography and allows detailed investigations of local Arctic climate conditions with a resolution never available before.

The Isfjorden region in central Spitsbergen is the most populated area of Svalbard. The settlements of Longyearbyen, Barentsburg and Pyramiden along its shoreline make it the most-trafficked fjord of the whole archipelago and human activity spreads all over the fjord system. Making use of the easy access via Svalbard Airport and the well-developed infrastructure, researchers of various scientific disciplines base their activities in Longyearbyen and utilize Isfjorden as a well-suited outdoor laboratory to study climate processes and their current changes in the Arctic. However, the atmospheric state does not only act as boundary condition on the physical-biological-geological interactions within the fjord system (Cottier et al., 2007; Descamps et al., 2017; Muckenhuber et al., 2016; Nilsen et al., 2016; Schuler et al., 2020; Skogseth et al., 2020; Tverberg et al., 2019; Walczowski & Piechura, 2011). The local weather conditions additionally set limits to all kinds of operations in the field. Hence, there is a strong interest to better understand the local climate conditions.

This study utilizes CARRA data to characterize the local micro-climate over Isfjorden, focusing on five major atmospheric variables: near-surface temperature, humidity and wind as well as total cloud cover and precipitation. Note that in order to limit the number of presented variables and the scope of the study, liquid and solid

precipitation are not explicitly distinguished. CARRA's high horizontal resolution allows spatial differentiation of sub-areas like the inner fjord arms or mountain ranges, that have so far not been resolved in previous atmospheric reanalysis data sets. In this way, we are able to provide a comprehensive overview of the climatic conditions in the region for scientists from a wide range of disciplines as well as to local operators of field activities, for example, in the tourism or fishing industry. From a larger perspective, these results will provide a detailed case study on the micro-climate of Arctic fjords and their impact on the surrounding land masses. In the following Section 2, we introduce the data used in this study and the methods we applied during the analysis. The main results are presented and discussed in Section 3. Finally, we summarize our findings in Section 4 and outline priorities for coming studies.

2. Data and Methods

2.1. CARRA

CARRA is developed in collaboration between several European weather services, with MET Norway as one of the main institutions responsible. It is produced using the HARMONIE-AROME non-hydrostatic regional NWP system (Bengtsson et al., 2017) and covers the time period 1990–2022 with a resolution of one hour (re-initialization every third hour). In the vertical dimension, the hybrid coordinate system includes 65 model levels where the lowest level is located at approximately 12 m above the Earth's surface and the highest level at 10 hPa (for more details see Müller et al. (2017) and Køltzow et al. (2019)). With a horizontal resolution of 2.5 km, CARRA resolves more local details than for example, the ERA5 global reanalysis (31 km grid spacing, Hersbach et al. (2020)), which is used as lateral boundary condition. The whole data set covers two domains. While the western domain includes Greenland, Iceland and the surrounding seas, the eastern domain relevant for this study has an extent similar to the domain of the operational AROME-Arctic NWP model run by MET Norway. It covers the European Arctic, including Svalbard, Franz Josef Land, Novaya Zemlya, large parts of Fennoscandia, the Barents Sea and the north-eastern Greenland Sea. Yang et al. (2020) provide the full product documentation.

Even though CARRA data is available from 1990, we only use data from June 2011–May 2021 in this study. This is due to the rather low resolution of the satellite-based sea surface temperature and sea ice concentration forcing data sets (compared to the spatial scales of the inner fjord arms of Isfjorden) used in CARRA before this time period. Further details on this issue can be found in Supporting Information S1. More information about the quality of the sea surface temperature can be found in Skogseth et al. (2020) and more technical details on the full system are provided by Yang et al. (2020)).

The investigated variables are 2 m air temperature (T2), specific humidity (Q2), 10 m wind speed (WS10), total cloud cover (TCC) and precipitation (PRECIP). For most variables considered, 3-hourly-analyses are extracted from the full data set for a region centered on Isfjorden (see Figure 1). Daily accumulated precipitation values are inferred as the difference between the 30-hr and 6-hr lead time forecasts. In addition to the surface fields, wind direction data from the 850 hPa pressure level (Schyberg et al., 2020a) are spatially averaged over the study area (see Figure 1) and grouped into eight sectors centered around the four cardinal and four ordinal directions. The resulting time series is used as a reference for the synoptic-scale flow direction in the statistical analyses. Even though the highest mountain peaks in the study area in reality reach heights close to the 850 hPa level, the model topography is smoothed due to the finite model grid resolution and the highest model grid point within the study area is located at only 929 m above sea level. It can therefore be assumed that the 850 hPa flow over the study region is sufficiently distanced from the underlying topography to be used to characterize the synoptic flow conditions. Model grid-referenced wind components are rotated to follow a regular geographic coordinate system. Subsequently, wind speed and direction are calculated following basic vector geometry. Low-level atmospheric static stability is quantified by the difference in potential temperature between 850 hPa and the surface (T2). As the available model output only includes 2 m relative humidity, Q2 is calculated from T2, relative humidity and surface pressure fields.

2.2. Statistical Analysis

For the analyses of this study, basic statistics are applied to T2, Q2, WS10, TCC and PRECIP. Annual variations and seasonality are investigated by binning the data set into monthly and seasonal (DJF, MAM, JJA, SON)

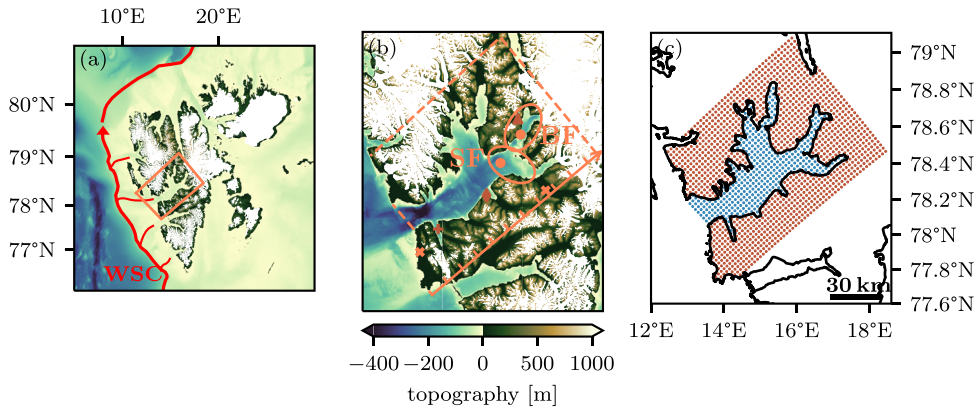

Figure 1. (a) Location of the study area and the West Spitsbergen Current (WSC, red arrows, based on Vihtakari et al. (2019)) in the Svalbard region. (b) Zoom into the study area. Four reference model grid points are marked with red markers in Sassenfjorden (SF), Billefjorden (BF), Sassendalen and at the west coast. The main settlements of Longyearbyen, Barentsburg and Pyramiden are indicated with a brown diamond, plus and triangle, respectively. The native y-axis-orientation of the CARRA model grid defining the axis for the calculation of along-fjord horizontal gradients is indicated with the arrow, including ticks defining the 5 km-wide bins. Glaciated areas are white-colored on top of the elevation color scheme. (c) Map covering the same area as (b), with the locations of model land grid points used in this study indicated in red and sea grid points in blue.

categories. Furthermore, the synoptic flow type at each time step is defined by the spatially averaged 850 hPa wind direction sector (see Section 2.1). In order to quantify horizontal gradients between the head (east) and the mouth (west) of Isfjorden, data is averaged over 5 km-wide bins along the axis defined in Figure 1. Model land and sea grid points are distinguished based on the model's own land-sea mask. Besides analyzing average fields of all five variables binned into the above-described categories, particular focus is put on their variability both in time and space. While temporal variability has been investigated in the past using observational time series, using the high resolution CARRA data set now allows for a direct comparison with its spatial counterpart. After grouping the time series into monthly and synoptic flowtype categories, the temporal variability for each group and at each grid point is defined as the standard deviation over all time steps within the respective group. The spatial variability per group is given by the temporally averaged standard deviation over all model grid points. Direct quantitative comparison is possible as the same metrics are used for spatial and temporal variations. Such a comparison puts in perspective the importance of spatial variations generated by the complex topography of the fjord environment.

3. Results and Discussion

3.1. Synoptic Flow

The distributions of the synoptic-scale flow directions in Figure 2 show substantial seasonal differences. During DJF, the total numbers are distributed rather equally over all directions. However, weak and medium wind speeds typically occur with northerly winds, while high wind speeds mostly coincide with wind from the southerly and easterly sectors. This pattern is even more pronounced in MAM, with northerly directions dominating the total

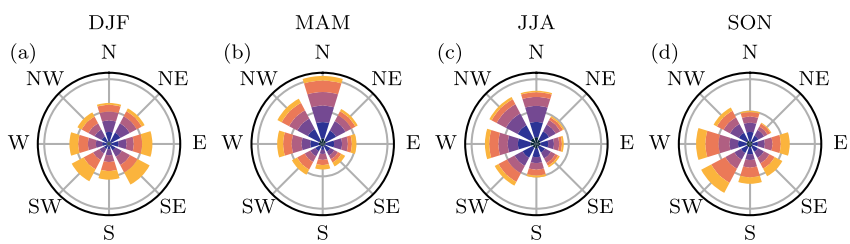

Figure 2. Seasonal mean wind roses of 850 hPa wind from CARRA, averaged over the whole Isfjorden area (see Figure 1). Wind speed categories (category thresholds 2.5, 4, 6, 8.5, 12 m s^{-1}) in color levels (blue = 2.5 m s^{-1}, yellow = 12 m s^{-1}).

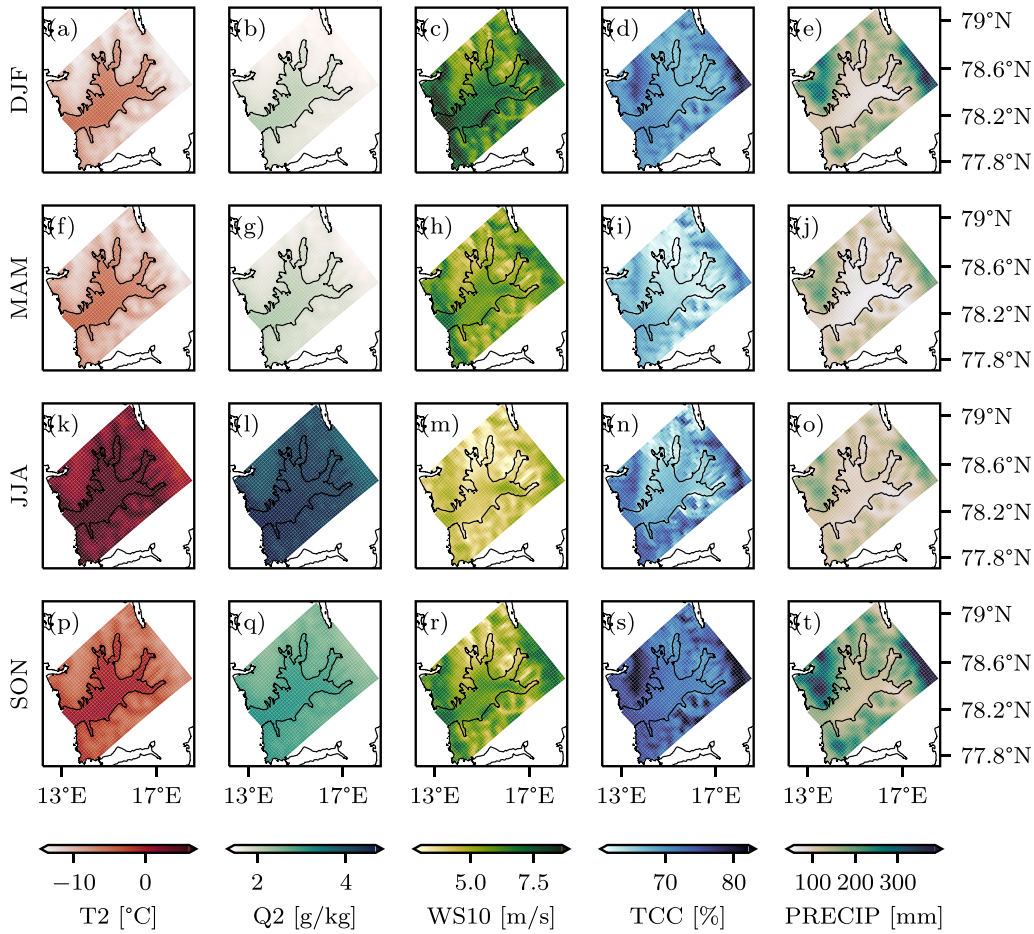

Figure 3. Seasonally averaged fields of the five investigated variables.

distribution (occurrence frequency 21%). A flow situation with weak to medium winds from the north over Isfjorden during winter and spring is typically established by a high-pressure system with its center over northern Greenland. This can be seen in the average large-scale mean sea level pressure (MSLP) fields corresponding to the seasonal and flowtype categories (see Figure S2 in Supporting Information S1). Strong southerly winds over Isfjorden are typically related to cyclone activity over the North Atlantic and the Fram Strait, which leads to winds with strong southerly components over Svalbard. In JJA, westerly directions are mostly dominating over easterlies (occurrence frequencies W: 16% compared to E: 8%). Low wind speeds are more abundant than in any other season. SON is a transition back to the winter type distributions. On one hand, westerly directions are still dominating in the total distribution (occurrence frequencies W: 17% compared to NE: 7%). On the other hand, high wind speeds occur more often again from the southerly sectors, indicating a seasonal increase in cyclone activity south and west of Svalbard during fall.

3.2. Local Climate Characteristics Overview

In the following, the local manifestation of the above-described synoptic-scale weather patterns over the Isfjorden region and their variations on seasonal time scales will be analyzed based on Figures 3–5. We provide additional, more detailed figures as Supporting Information S1. These further account for the seasonal variations in the occurrence frequencies of the synoptic flow conditions and present insights into the temporal variability.

As expected, T2 exhibits a strong seasonal cycle. Monthly mean T2 values are lowest in March (sea −8.9°C, land −13.9°C, see Figure 5), while the minimum T2 values drop to −34.0°C over land and −27.5°C over the fjord. These extreme cold events typically coincide with northerly synoptic-scale flow. The warmest month of the year is July, with a monthly mean T2 of 6.3°C over the fjord (over land: 4.7°C, see Figure 5). Spatially averaged

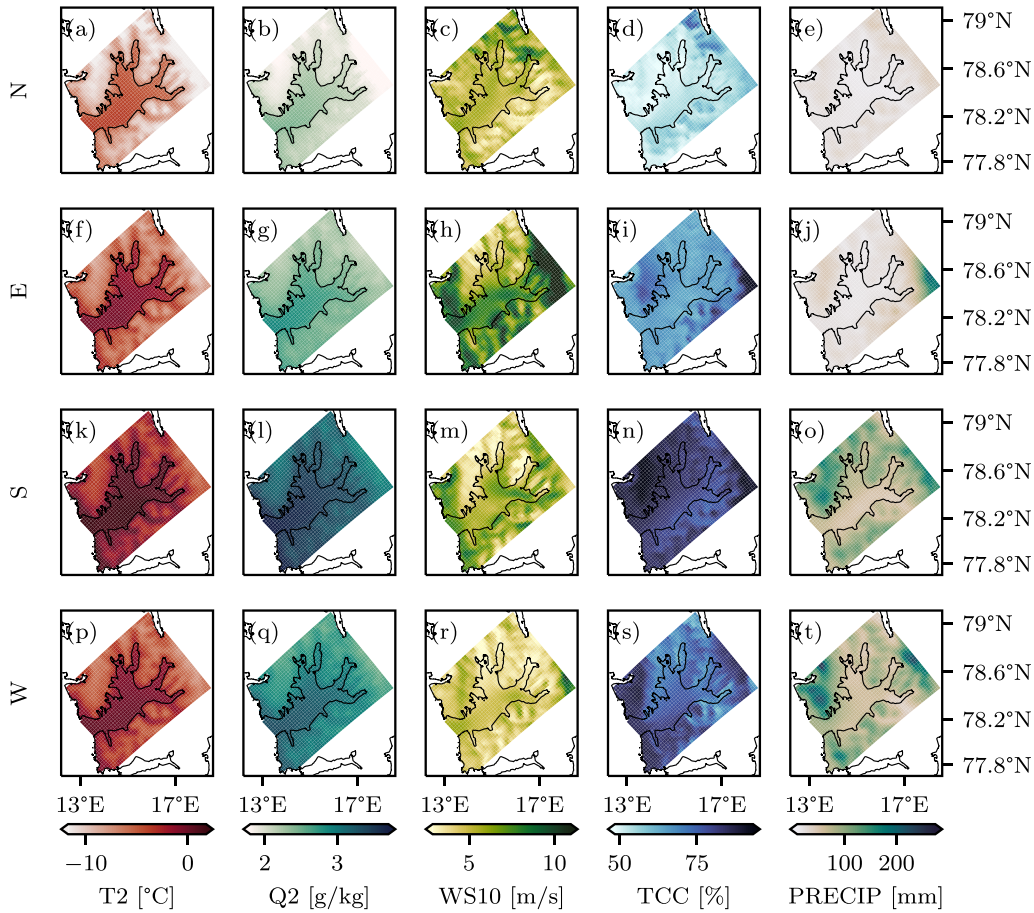

Figure 4. Average fields of the five investigated variables for the four cardinal synoptic-scale flow directions.

maximum T2 can rise to up to 14.6°C, typically during periods with southerly synoptic-scale flow. As the model land grid points are distributed over a wide range of topography heights, a spatial average over these land grid points is always also a vertical average over all topography heights. Therefore, a more detailed comparison of T2 over land and over the fjord, considering the vertical dimension, can be found in Section 3.3.3. Furthermore, the effect of Isfjorden acting as a heat island surrounded by colder (warmer) land masses during winter (summer) (see Figure 3) is quantified in Section 3.3.1.

A similar feature is seen in the Q2 fields, which show the fjord as an area of increased atmospheric humidity, especially during winter and spring (see Figure 3, further details can also be found in Section 3.3.1). The variations with respect to both season as well as synoptic-scale flow direction follow those seen in T2, with lowest values in winter/early spring (monthly mean March: sea 1.6 g kg^{-1}, land 1.3 g kg^{-1}, see Figure 5) and during northerly flow, and highest values in summer (July: sea 4.9 g kg^{-1}, land 4.7 g kg^{-1}) and during southerly flow, respectively. Horizontal gradients over the fjord area are small, but do slightly increase during summer (higher Q2 toward the mouth area of Isfjorden, see Figure 3 and details in Section 3.3.5).

The seasonal cycle seen in WS10 has an opposite structure compared to those in T2 and Q2, with highest values during the storm season in winter (see Figure 5). Spatially averaged maximum WS10 over sea (land) reach 25 m s^{-1} (27 m s^{-1}) in December. These maxima are related to low-pressure systems located in the Barents Sea south of Svalbard, setting up strong easterly and south-easterly flow over the Isfjorden region (see the MSLP maps provided as Figure S2 in Supporting Information S1). This synoptic-scale flow is modified by the topography surrounding the fjord, which leads to large horizontal as well as vertical gradients in the local wind field. Typically, the highest WS10 values are found at the high-altitude areas east and north-west of Isfjorden (see Figures 3 and 4). The overall dependence of WS10 on altitude is analyzed in Section 3.3.3. In the lee of the large mountain ranges mentioned above, areas with relatively calm mean conditions are present. This shows how the

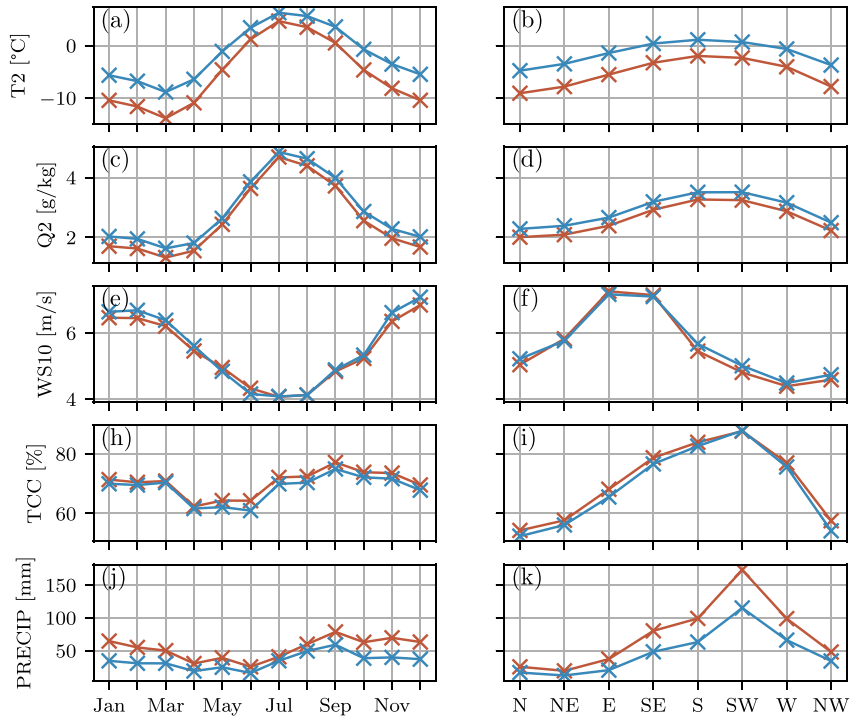

Figure 5. Average values of the five investigated variables, binned into monthly and synoptic flowtype categories, calculated separately for sea grid points (blue) and land grid points (red).

upstream topography blocks the flow. In contrast, when the flow aligns with valley or fjord axes, winds get channeled along those axes and local wind speeds can vary by several m s^{-1} over short distances. The most dominant example of such a channeling effect is the fjord jet developing over Sassenfjorden in the inner part of Isfjorden during periods with E–S synoptic flow (see Figure 4 and Section 3.3.2 for further details).

TCC over the study area is found to be mostly dependent on the direction of synoptic-scale air mass advection, with spatial averages of almost 90% for southerly and westerly flow transporting warm and moist air masses to Svalbard, compared to approximately 50% during periods with northerly flow, when cold and dry air from the central Arctic dominates (see Figure 5). As northerly flow types are more frequent, especially during spring, a corresponding seasonal cycle is present in the data. Locally over the fjord, the inner side arms are on average a bit less cloudy than the mouth area, which is more influenced by air masses and clouds forming over Fram Strait due to the warm Atlantic Water of the WSC (see Figure 1). This horizontal gradient is therefore more pronounced during westerly flow (see Figure 4). Over land, high-altitude areas are on average associated with increased cloudiness (details in Section 3.3.3).

Given that both Q2 as well as TCC are highest during southerly synoptic flow, it comes as no surprise that also most PRECIP is linked to southerly flow directions. In terms of seasonality, this translates into September being the wettest month of the year, with on average 79 mm (over land, 59 mm over the fjord), while June is the driest with only 25 mm (16 mm over the fjord) (see Figure 5). Again, the topography surrounding Isfjorden introduces large horizontal gradients. The high mountain ranges in the east and north of the mouth of Isfjorden exhibit substantially more PRECIP than low-altitude areas (see Figure 4 and Section 3.3.3 for more details). Similar to the lee effects of topography on WS10 and TCC, maximum PRECIP values can be found mainly upstream of the highest peaks.

3.3. Temporal and Spatial Variability

3.3.1. Fjord Heat and Moisture Island

Due to the large heat capacity of water and a slower exchange rate of the water masses inside Isfjorden (on the order of months to years, estimated based on information from Nilsen et al. (2008) and Skogseth

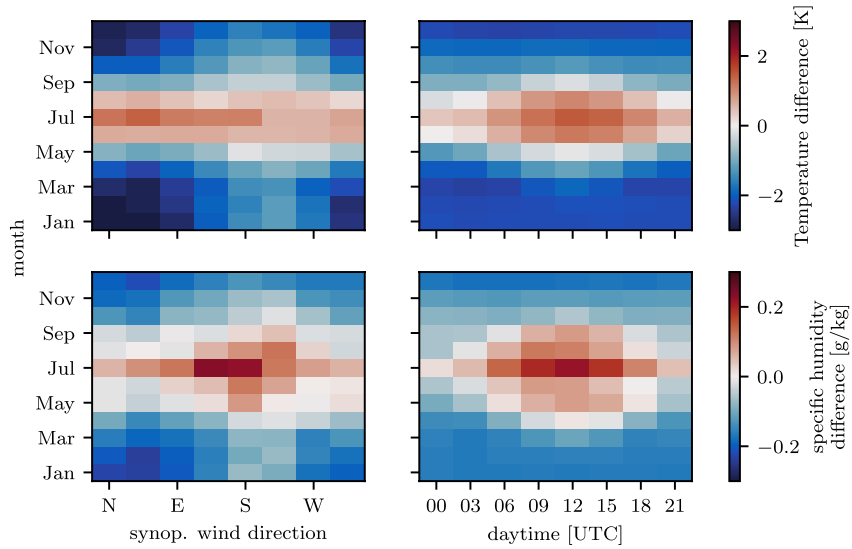

Figure 6. Difference in T2 and Q2 between spatially averaged sea grid points and land grid points lower than 100 m, for different synoptic wind directions (left column) and different times of the day (right column). Positive values indicate higher T2/Q2 over land than over the sea.

et al. (2020)) compared to the air masses above, seasonal changes in the sea surface temperature (SST) of the fjord are typically lagged with respect to air temperatures by 1 to 2 months (Byers, 1974; Li et al., 2013; Prescott & Collins, 1951). Furthermore, sea ice formation sets a natural lower limit to the range in SST, and the presence of sea ice or snow in summer sets an upper limit for the surface temperature. These limitations are not imposed to atmospheric temperatures. Taken together, these factors lead to seasonally large temperature differences between the fjord's surface and the air mass above, which in turn give rise to strong sensible (and latent) heat fluxes and local warming/cooling of the atmosphere. The resulting temperature difference between T2 over the fjord compared to T2 over land at sites no more than 100 m above sea level is largest during winter, when the fjord acts like an island of heat surrounded by colder land masses (see Figures 3 and 6). The magnitude of this temperature difference during winter strongly depends on the direction of the synoptic-scale flow, with largest values of up to −3 K for northerly flow, compared to only approximately −1 K during periods with southerly flow. In summer, when T2 typically rises above the SST, the gradient reverses and the air over land warms up to 2 K more than the air over sea. This is mostly independent of the direction of the synoptic-scale flow, presumably due to the generally largely decreased (temporal) variability during summer (for details see Section 3.3.5). However, on diurnal time scales, the seasonal land-sea contrast shows largest variability during summer, while there is no diurnal variation seen in winter. This shows that, even though the sun is up all day during summer, the warming of the land is strongly dependent on its elevation above the horizon.

Besides its impact on the local T2, the fjord also provides a large reservoir for atmospheric moisture. It has been known for decades that in winter, evaporation is large over open sea in the Arctic (e.g., Vihma, 2014). However, the concept of associated localized moisture islands has received little attention compared to that of heat islands, presumably because the inclusion of phase changes presents a challenge for idealized model studies. Outside the Arctic, localized elevated humidity levels have been studied mainly in the context of urban heat/moisture islands (e.g., Kuttler et al., 2007; Lokoshchenko, 2017; Richards, 2005; Wang et al., 2021), with varying results regarding the moisture difference between urban and rural sites. Using CARRA, we can statistically characterize the moisture island over Isfjorden in the same way as the heat island. During winter and spring, elevated Q2 levels are found over the fjord compared to over land (maximum difference with northerly synoptic-scale flow during December: 0.2 g kg^{-1}). Like for T2, a dependency is present only on the synoptic-scale flow direction, but not on the time of day. In summer, the gradient between Q2 at land and sea grid points reverses (similar to T2), with an average Q2 up to 0.2 g kg^{-1} higher over land than over the fjord (during southerly synoptic-scale flow and around noon). This suggests that sufficient moisture sources are available also over land and Q2 is mainly controlled by the temperature dependency of the saturation water vapor pressure.

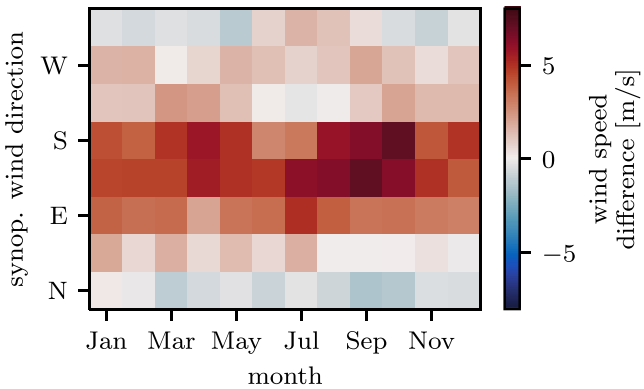

Figure 7. WS10 difference between the two reference grid points in Sassenfjorden and Billefjorden (see Figure 1, binned into months and synoptic flowtype. Positive values indicate higher WS10 in Sassenfjorden than in Billefjorden.

3.3.2. Fjord Jet

Due to the surrounding topography, near-surface winds in mountainous areas like Svalbard frequently get channeled along the valley and fjord axes.

In the following, we look at an example case and quantify this effect on WS10 as the WS10 difference between Sassenfjorden (axis NW–SE, see Figure 1) and Billefjorden (axis SW–NE). Figure 7 shows that during periods with synoptic-scale flow from easterly to southerly directions (along the Sassenfjorden axis and perpendicular to the Billefjorden axis), the average WS10 over Sassenfjorden can be up to 7 m s^{-1} higher than in the adjacent Billefjorden. In turn, increased wind speeds are seen over Billefjorden compared to Sassenfjorden during periods with northerly winds (maximum difference of 1.5 m s^{-1} in September). Interestingly, it appears that the peak of wind speed maxima over Sassenfjorden shifts from periods with easterly synoptic flow direction during summer toward more southerly directions during winter and the shoulder seasons (MAM and SON). Furthermore, the peak in WS10 difference for reversed flow (synoptic-scale W–NW) is only seen during summer (see Section 3.1). These findings could be a consequence of more pronounced stable boundary layers over the fjord during summer than during winter, forcing the near-surface flow to follow the topographical restrictions to a larger extent (see e.g., Esau and Repina (2012). No diurnal variations are present in these findings (not shown).

Obviously, Sassenfjorden is not the only place where such a fjord (or valley) jet can develop. The respective Figure S5 addressing WS10 in Supporting Information S1 shows lots of small-scale variability in the near-surface wind fields, connected to the complex topography surrounding Isfjorden. Unfortunately, due to its limited horizontal resolution (2.5 km), CARRA can only resolve the larger features. Nevertheless, the results presented here give a good indication of the magnitude as well as the variability of WS10 enhancements due to topographical channeling in general and similar patterns can be expected for other locations in Svalbard.

3.3.3. Orographic Gradients

The high horizontal grid resolution of CARRA allows investigations of spatial gradients in the five atmospheric variables due to the orography around Isfjorden. In the blue axes in Figure 8, these near-surface gradients are presented as functions of the height above sea level and are in the following referred to as orographic gradients.

Figures 8a and 8b show these orographic gradients in T2. Throughout the year, the domain-averaged orographic gradient corresponds to a statically weakly-stable stratification lapse rate of approx. 8–9 K km^{-1}, with an increasing tendency towards more positive values at the highest altitudes. This increase in stability can be explained with enhanced cloud formation at higher altitude (see further analysis below) and the corresponding latent heat release.

Mean WS10 at high-altitude areas is on average increased by 1–2 m s^{-1}, compared to lower height levels, throughout the year. This effect is more strongly pronounced during easterly synoptic flow. For the interpretation of this finding, one must keep in mind the limited data availability at height levels above approximately 700 m and the location of these high-altitude areas to the east of the fjord (exposed to the easterlies, see Figure 4). For all seasons and most synoptic-scale flow directions, a small but consistent peak of the average WS10 in the lowest altitude range can be seen. This signal mainly originates from the flat open areas along the west coast (not shown), where topographic effects are small. As already mentioned above, TCC is largest at high altitudes (increased by up to 15% compared to values around 200 m altitude), due to lifting condensation, cloud formation and trapping of clouds below inversion layers. A secondary peak in the lowest height levels indicates near-surface clouds and fog getting trapped in the valley bottoms and at the mountain ranges along the west coast. While this vertical structure is largely independent of seasonal variations, the high-altitude TCC increase is largest during easterly synoptic flow periods (mostly due to local maxima in the high-altitude areas around the innermost fjord arms, see above). In contrast, the cloud/fog layer near the surface mostly forms during westerly flow and along the foot of the coastal mountain ranges. Orographic gradients in the PRECIP profiles are of the order 10 larger than their horizontal counterparts. During fall/winter and southerly synoptic flow (the seasons/flow directions with the largest absolute values in PRECIP, see Section 3.2), the orography-induced gradients exhibit increases of

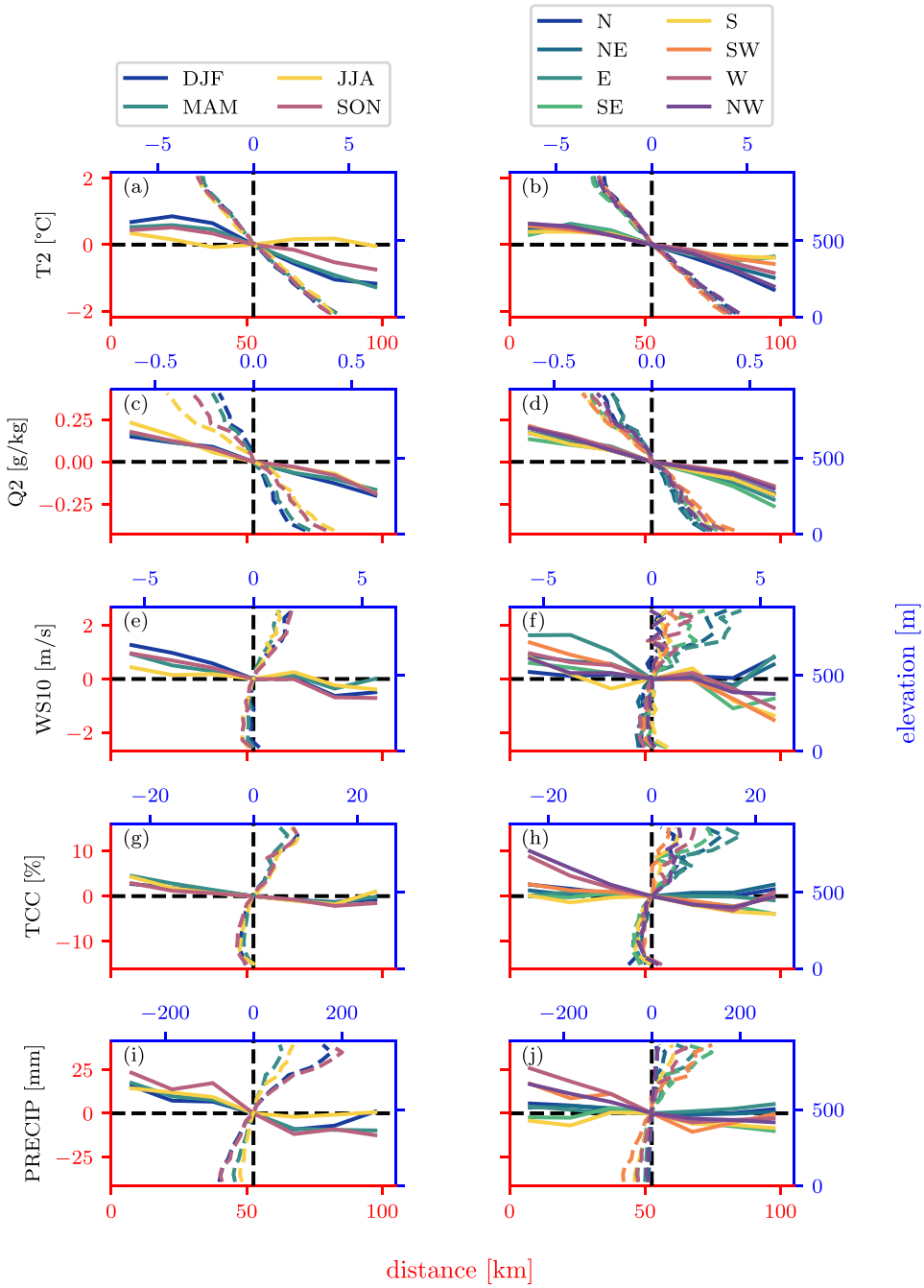

Figure 8. Horizontal (solid curves, red axes) and orography-induced gradients (dashed curves, blue axes) in major atmospheric variables. The horizontal gradients are calculated based on sea grid points only, binned into 5-km-wide sections along CARRA's native *y*-axis (see Figure 1). The data for each height level is calculated as the spatial average over all land model grid points within 50-m-topography-height intervals. Both horizontal and orography-induced gradients are normalized with respect to their respective central bin (50 km/500 m) and further divided into seasonal as well as synoptic-flow direction categories.

more than 200 mm from sea level to 1,000 m. In contrast, the gradients during northerly synoptic flow are small. However, in relative units, PRECIP doubles from sea level to approximately 700 m, independently of season or synoptic flow direction.

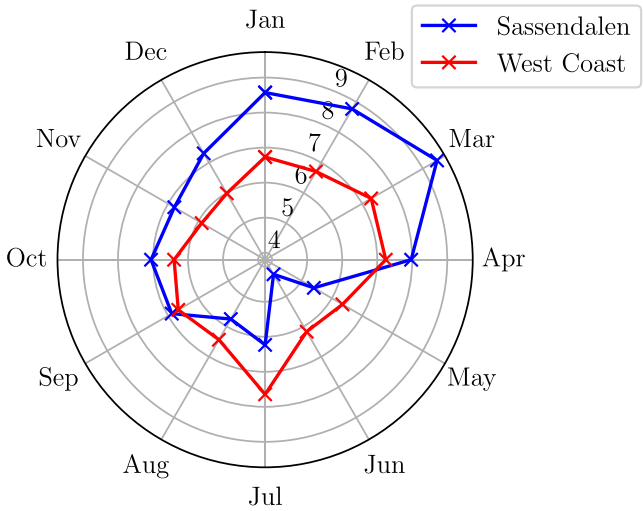

Figure 9. Seasonal variability in the difference in potential temperature between 850 hPa and the surface for two example locations at the west coast and in Sassendalen (see Figure 1). The unit of the radial axis is K.

3.3.4. Along-Fjord Horizontal Gradients

Using long-term meteorological monitoring, for example, from Longyearbyen Airport or Isfjord Radio, several studies have already investigated the temporal variability of the atmospheric variables considered in this study (e.g., Hanssen-Bauer et al., 2019; Isaksen et al., 2016). Spatial variability has so far been investigated as horizontal gradients, especially in T2, between the same observational sites (e.g., Gjelten et al., 2016; Skogseth et al., 2020). We calculate horizontal gradients of selected variables over Isfjorden (only sea grid points) along an axis directed from the mouth of the fjord toward its head in Billefjorden (see Figure 1) to quantify the spatial variability in a similar way and compare the results with findings from previous, observation-based studies. Figure 8 (a) and (b), red axes, show horizontal variations in T2, normalized by the central distance bin. The mouth area in the south-west (beginning of the transect) is on average approximately 0.5 K warmer than the central fjord. This is due to the strong maritime influence of the open ocean in Fram Strait to the west and the warm Atlantic Water in the WSC (Figure 1). This deviation is strongest in winter, but virtually independent from changes in the synoptic flow direction. The inner fjord arms in the north-east are covered by sea ice during winter and spring and additionally more strongly influenced by the surrounding land. During winter and the shoulder seasons, T2 is about 1 K lower over these fjord arms than over the central fjord, while in the summer, differences are negligible. These values are in good agreement with results from Gjelten et al. (2016).

The increasing maritime characteristics of the fjords' micro-climate toward the open ocean in the west also impacts adjacent low-elevation land areas. Around the inner fjord arms, especially those with sea ice cover during winter and spring, strong radiative cooling and resulting drainage flows lead to the formation of cold pools and surface-based inversions in the valley bottoms (Vihma et al., 2011). The resulting low-level thermal stratification maximum can be seen in Figure 9 in form of the difference in potential temperature between 850 hPa and the surface for an example grid point in Sassendalen (grid point elevation: 31.8 m) (see Figure 1), which is taken to represent the conditions in the valleys adjacent to the inner fjord arms. In contrast, the flat low-altitude areas along the west coast (elevation of respective example grid point: 10.9 m) are strongly impacted by the relatively warm surrounding water masses, hence cold pools and near-surface inversion layers are less likely to form during winter. Similarly, during summer, the large heat capacity of the open ocean dampens T2 maxima along the west coast, while air temperatures in the valleys further inland increase more strongly, leading to a decreased thermal stratification close to the surface.

Along-fjord atmospheric temperature variations naturally also have an impact on the mixed layer depth evolution in the ocean and consequently the potential for sea ice formation in the inner side fjords compared to Isfjorden proper. Due to the elevated atmospheric temperatures during summer, the warming of the side-fjords' mixed layer is stronger than in Isfjorden proper. Consequently, this additional heat needs to be released again during fall and winter, before sea ice can form.

Besides variations in T2 and the corresponding near-surface static stability, we additionally present similar analyses for all other variables addressed in this study. Horizontal gradients in Q2 largely follow those in T2 and vary mostly on seasonal time scales. WS10 variations are more dependent on the synoptic flow direction. Figures 4h and 8f show how Isfjorden mouth is more prone to increased wind speeds during all synoptic conditions, but especially during periods when the wind aligns with the main fjord axis (SW–NE). In a similar way, the innermost fjord arms exhibit increased wind speeds during N–E synoptic flow. With differences between the inner-/outermost fjord arms and the reference in the center of the fjord on the order of 1–2 m s^{-1}, this underlines the importance of local channeling effects on WS10 described in Section 3.3.2. On average throughout the year, TCC is found to be higher in the mouth area than in the inner fjord arms, as air masses advected from the Fram Strait during westerly synoptic flow are typically warm and moist. During easterly flow, the spatial gradients are small or might even reverse and TCC is largest in the eastern parts of the fjord, due to clouds getting trapped between mountain ranges over the inner fjord arms. PRECIP values are increased by up to 40 mm/season in the

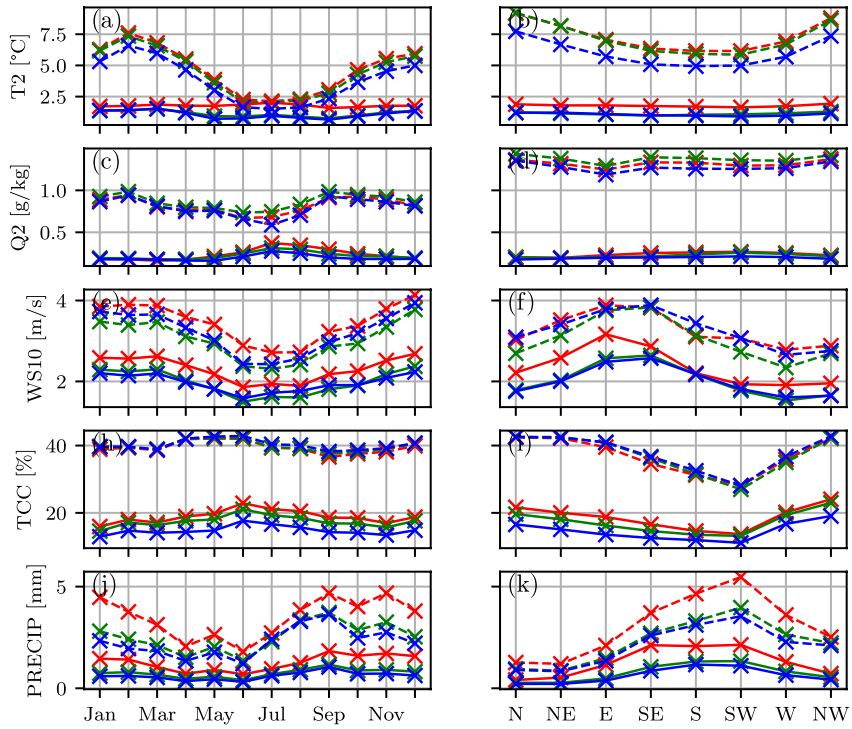

Figure 10. Comparison of spatial (solid curves) and temporal (dashed) variability (given by the respective standard deviations) calculated separately for sea grid points (blue), land grid points at elevations less than 100 m (green) and higher than 100 m (red).

mouth area compared to the inner fjord arms. This gradient is present during all seasons, but especially with westerly synoptic flow, when moist air masses from the Fram Strait get pushed against the coastal mountains, resulting in topography-induced precipitation. All these findings together show the gradient from more maritime climatic conditions in the south-west highly influenced by the warm Atlantic Water of the WSC, compared to more continental climate conditions in the inner parts of the fjord system.

3.3.5. Spatial Versus Temporal Variability

The spatial coverage of the CARRA data set together with its high horizontal resolution for the first time allows to calculate the magnitude of the total spatial variability over the whole Isfjorden region (standard deviation over model grid points, see Section 2.2) and compare it to its temporal counterpart. This analysis gives valuable information on what can be expected when traveling in the fjord system at a particular time as well as the variability expected in air-sea interaction within the fjord and further, how this will impact sea ice formation and water mass transformation in the fjord system. Figure 10 compares spatial to temporal variability of the five investigated atmospheric variables, separating land from sea points and binning the results into monthly as well as synoptic-scale flow direction categories.

The first factor to notice is that all five variables feature variability dependent on both season and synoptic-scale flow type. Furthermore, the spatial variability is generally smaller than the temporal variability but both temporal and spatial variability tend to be larger over land than over the fjord. This is due to the impact of the topography and varying surface cover over land, as well as due to the higher heat capacity of water. In order to distinguish these different effects, results are presented separately for land grid points at elevations lower and higher than 100 m.

Temporal variability of T2, Q2, and WS10 roughly halve during summer, compared to winter, as the weather systems slow down due to the reduced meridional temperature gradient between the Arctic and the mid-latitudes. For T2, that means that the temporal variability reduces to levels of spatial variability. Lowest temporal variability in PRECIP occurs earlier during spring, coinciding with the minimum in total PRECIP itself. In contrast, TCC variability shows a small increase at that time of the year. Differences in the spatial variability of T2 between

summer and winter are far less pronounced than in the temporal variability, with only a slight dip in variability over the fjord. Spatial variability of Q2 and TCC increases during summer for both the fjord and the surrounding land, while WS10 and PRECIP exhibit maximum variability during late fall and winter, reaching levels of their respective summer/fall temporal variability. It is interesting to note that the elevated spatial variability in Q2 is an exception from the general tendency of Q2 to follow T2. This is likely a consequence of the exponential dependence of the saturation water vapor pressure on temperature, meaning that high temperatures during summer also lead to higher specific humidity values than during winter, which in turn leads to larger absolute spatial differences.

Except for a drop in T2 temporal variability during periods with southerly synoptic-scale flow, T2 and Q2 variability is virtually independent of the synoptic-scale flow direction. For the remaining three variables, the found dependencies are similar for spatial and temporal variability. WS10 variability increases by approximately 1 m s^{-1} during periods with easterlies compared to westerlies, with spatial variability reaching similar levels to temporal variability in westerlies. As the eastern part of the study area is dominated by high mountain ranges, easterly flow is strongly altered by the topography, resulting in elevated variability levels. In contrast, westerly flow is less impacted by topography, as it is coming from the open sea in the Fram Strait. For TCC, the most variable conditions take place with northerly synoptic flow, while during south-westerly synoptic-scale flow (which coincides with the highest values of absolute TCC, see Section 3.2), variability is minimal. PRECIP variability is, in contrast, largest with south-westerly synoptic flow and the maximum of the spatial variability peaks at values similar to minimal temporal variability. Furthermore, the difference between land and sea grid points is substantially increased compared to other synoptic flow conditions.

In the case of WS10 and PRECIP, the general drop in variability (both spatial and temporal) over the fjord compared to the surrounding land can mainly be attributed to topographic effects, as the results for low-elevation (below 100 m above sea level) land points largely resemble the ones for sea grid points. In contrast, the drop in TCC spatial variability over the fjord is more closely related to the fjords' large heat capacity, considering that the results for low- and high-elevation spatial variability have very similar values. T2 and Q2 exhibit mixed signals. While the drop in their respective temporal variability over the fjord is mainly caused by the thermal properties of water compared to land surface, the increased spatial variability over land is more closely linked to topographic effects, following the same argumentation as above.

In addition to comparing the spatial variability to its total temporal counterpart, a similar analysis was performed looking at the temporal variations on diurnal time scales. It was found that diurnal variations are very small for most variables, seasons and synoptic flow directions. Only the diurnal cycle in T2 is associated with variations similar in magnitude to the respective spatial variability. Therefore, it was chosen to not include the respective additional data points in Figure 10.

4. Summary and Conclusions

Using the new CARRA reanalysis, the present study provides climatologies of five key atmospheric variables over Isfjorden, Svalbard. The findings confirm different aspects of previous work on climatic conditions in Svalbard, for example, the impact of different synoptic situation on the local climate (Wickström, Jonassen, Cassano, & Vihma, 2020) and the temperature gradient between the head and mouth of Isfjorden (Gjelten et al., 2016). Making use of the high spatial resolution of CARRA with grid points distributed equally over the whole study area, particular attention was drawn to phenomena related to the complex topography surrounding Isfjorden.

During different seasons and synoptic-scale flow, the climatic conditions in the mountain ranges around Isfjorden partly differ substantially from those at sea level. Average orographic temperature gradients were found to be sub-adiabatic, corresponding to conditionally stable stratification. TCC is found to be strongly increased in high-elevation regions during easterly synoptic-scale flow. Seasonal PRECIP typically doubles from sea level to approximately 700 m height, with the largest absolute differences between low and high elevations occurring during periods with southerly synoptic-scale flow in fall and winter.

The fjord jet developing over Sassenfjorden is the most prominent example of how near-surface winds get channeled along fjord (and valley) axes and local wind speeds vary by several m s^{-1} over small horizontal distances. These channeling effects are seen in many places of the study area. However, CARRA's horizontal grid spacing of 2.5 km is still not sufficient to properly capture the effect of the smaller valleys and fjords on the flow fields.

Valkonen et al. (2020) indicate how a sub-kilometer NWP system can improve weather forecasting in the complex terrain of Svalbard. In the same way, a sub-kilometer reanalysis would allow to statistically investigate features in the flow fields on scales similar to the characteristic dimensions of the topography in the Isfjorden region.

During winter, Isfjorden is a heat and moisture island with increased T2 and Q2 levels, compared to the surrounding land. In summer, the gradient reverses in both variables. These fjord heat and moisture islands impact adjacent low-elevation areas especially in the southern and western parts of the fjord system, leading to relatively low (high) near-surface temperatures during summer (winter). In contrast, cold pool formation due to strong radiative cooling and resulting drainage flows during winter dominate the valley bottoms further inside the fjord system. Both effects represent deviations from the average orographic temperature gradient. A climatology based on point measurements from weather stations located around Isfjorden (e.g., the MET Norway station at Svalbard Airport) might therefore not be representative for neither the fjord nor the surrounding land, as they measure a mixture of the fetch from both types of areas. A new network of weather stations operated by the University Centre in Svalbard and installed all around Isfjorden and on-board ships sailing across the fjord will give valuable insights into this small-scale spatial variability in the future (Frank et al., 2023).

A direct comparison of the total temporal and spatial variability of near-surface air temperature and humidity, wind speed, total cloud cover and precipitation shows that in general (a) the spatial variability over land is larger than over the fjord, (b) the spatial variability is smaller than the total temporal variability, but (c) the spatial variability is larger than the diurnal cycle. Seasonal differences and dependencies on the synoptic-scale flow direction introduce variations on the same order of magnitude as the total temporal and spatial variability within a season. These findings provide valuable insight for the planning and safety of all kinds of field activity in the Isfjorden region.

On seasonal to inter-annual time scales, the Arctic Oscillation (AO), the North Atlantic Oscillation (NAO) and the Scandinavian Pattern (SCAND) are key climate indices used to describe the prevailing weather conditions in Scandinavia and the European Arctic (respective time series not shown here, but can be found e.g., at https://www.ncei.noaa.gov/access/monitoring/nao/, https://www.ncei.noaa.gov/access/monitoring/ao/ and https://www.cpc.ncep.noaa.gov/data/teledoc/scand.shtml). Wickström, Jonassen, Vihma, and Uotila (2020) show that especially the SCAND is correlated with the winter cyclone activity in the Svalbard region, which in turn naturally impacts the local weather conditions experienced in the Isfjorden fjord system. Furthermore, inter-annual variability in local atmospheric temperatures is closely linked to the inflow of Atlantic Water from the WSC into Isfjorden (Skogseth et al., 2020). The increasing fjord heat content together with low sea ice cover during the study period give rise to stronger heat exchange between the fjord and the atmosphere above. Addressing the question how the Atlantic Water enters Isfjorden in the first place, Nilsen et al. (2016) suggested a two-step-mechanism: First, southerly winds on the West Spitsbergen Shelf force Atlantic Water from the WSC to penetrate onto the shelf and toward the mouth of Isfjorden as the Spitsbergen Trough Current (Nilsen et al., 2016). At this point, northerly winds are needed to slow down the coastal current, which usually acts as a geostrophic barrier for Atlantic Water to enter Isfjorden, and by that eventually open the fjord and allow the Atlantic Water to enter. In addition, these northerly winds will lead to an Ekman transport away from the West Spitsbergen coast and subsequently upwelling of Atlantic Water from lower layers directly in the Isfjorden mouth region. Section 3.1 of this study shows how northerly winds dominate over Isfjorden in spring during recent years. This matches the above-described opening mechanism leading to the increased Atlantic Water inflow as reported by Skogseth et al. (2020). A more in-depth analysis of connections between the inflow of Atlantic Water into Isfjorden and atmospheric forcing, for example, related to the aforementioned climate indices, would be pertinent but has not yet been carried out and is beyond the scope of this study.

In terms of limitations of the CARRA data set, it is clear that, in spite of its relatively high horizontal grid resolution (2.5 km), there are still complex topographic features in the study region that are not fully resolved, as outlined above. Furthermore, the sparse observational network in the region does not allow for an assessment of the representativeness error (as was done by Køltzow et al. (2022) for mainland Norway). One can therefore not conclude on the spatial variability on scales smaller than the model resolution for the study area. Furthermore, it is known that parameterizations of subgrid-scale processes related to for example, stable boundary layers present challenges to NWP models, especially in the Arctic (Køltzow et al., 2019; Zilitinkevich & Esau, 2005). Therefore, uncertainties in the results of this study can be expected to be larger for low-elevation land areas during winter, when these stable boundary layers regularly form (see Section 3.3.4). Nevertheless, in spite of

uncertainties in the CARRA data, such as those outlined above, the data set does validate well against available observations (Køltzow et al., 2022) and performs better than for example, ERA5. It is therefore still believed that the general findings on the atmospheric conditions and their relative differences between areas within the study region (including land and sea grid points) and synoptic conditions are robust and representative of reality.

Regarding the major atmospheric variables considered, the scope of this study has for brevity been limited to five major ones and precipitation has only been treated in its total form. It is worth noting, however, that precipitation might have very different impacts during the different seasons, depending on its type. For instance, precipitation falling as rain on snow covered ground during winter (so-called rain-on-snow), will typically have a very different (and potentially detrimental) impact on for instance transport and tourism as well as terrestrial ecosystems compared to precipitation falling as snow-on-snow (Descamps et al., 2017).

Fjord systems similar to Isfjorden can be found all around the Arctic, especially in Greenland and the Canadian Archipelago. Their lengths are typically on the order of 100 km, their widths on the order of 5–10 km and their main basins reach depths on the order of several hundreds of meters. They are at least partly sea ice covered during parts of the year and surrounded by large glaciated areas in close proximity, including marine-terminating glaciers calving into the inner fjord arms. The surrounding permafrost tundra is typically snow covered during winter and spring, but snow free during summer and is dominated by mountainous landscapes. The present study demonstrates the added value of an atmospheric high-resolution regional reanalysis like CARRA for studies of phenomena related to the local topography and the land-sea contrast and their impact on the micro-climate in these types of regions. Its findings serve as indicator for the micro-climatic conditions in Isfjorden and similar fjord system elsewhere, also those presently not covered by a high-resolution reanalysis product. Furthermore, it has been argued how local atmospheric winds are forcing other components of the climate system, especially the fjord itself. Together with future work focusing on the air-sea-ice interaction within the fjord and implications for the local sea ice production and water mass transformation, these results act as a proxy for similar processes taking place in other fjords all around the Arctic.

Data Availability Statement

The CARRA near-surface (Schyberg et al., 2020b) and pressure level data (Schyberg et al., 2020a) as well as the ERA5 MSLP data set included in Supporting Information S1 (Hersbach et al., 2018) are available online at the Copernicus Climate Change Service Climate Data Store.

Acknowledgments
The Copernicus Climate Change Service Climate Data Store and specifically the Norwegian Meteorological Institute and the ECMWF are acknowledged for providing the CARRA and ERA5 data, respectively. The work of Timo Vihma was supported by the European Union's Horizon 2020 research and innovation framework programme under Grant agreement no. 101003590 (PolarRES project).

References

Bengtsson, L., Andrae, U., Aspelien, T., Batrak, Y., Calvo, J., de Rooy, W., et al. (2017). The HARMONIE–AROME model configuration in the ALADIN–HIRLAM NWP system. *Monthly Weather Review*, *145*(5), 1919–1935. https://doi.org/10.1175/mwr-d-16-0417.1

Boyd, T. J., & D'Asaro, E. A. (1994). Cooling of the West Spitsbergen Current: Wintertime observations west of Svalbard. *Journal of Geophysical Research*, *99*(C11), 22597–22618. https://doi.org/10.1029/94jc01824

Bromwich, D. H., Wilson, A. B., Bai, L.-S., Moore, G. W., & Bauer, P. (2016). A comparison of the regional Arctic system reanalysis and the global ERA-interim reanalysis for the Arctic. *Quarterly Journal of the Royal Meteorological Society*, *142*(695), 644–658. https://doi.org/10.1002/qj.2527

Byers, H. R. (1974). *General meteorology (tech. Rep.)*. McGraw Hill.

Carmack, E., Polyakov, I., Padman, L., Fer, I., Hunke, E., Hutchings, J., et al. (2015). Toward quantifying the increasing role of oceanic heat in sea ice loss in the new Arctic. *Bulletin of the American Meteorological Society*, *96*(12), 2079–2105. https://doi.org/10.1175/bams-d-13-00177.1

Cottier, F., Nilsen, F., Enall, M. E., Gerland, S., Tverberg, V., & Svendsen, H. (2007). Wintertime warming of an Arctic shelf in response to large-scale atmospheric circulation. *Geophysical Research Letters*, *34*(10), L10607. https://doi.org/10.1029/2007GL029948

Dahlke, S., Hughes, N. E., Wagner, P. M., Gerland, S., Wawrzyniak, T., Ivanov, B., & Maturilli, M. (2020). The observed recent surface air temperature development across Svalbard and concurring footprints in local sea ice cover. *International Journal of Climatology*, *40*(12), 5246–5265. https://doi.org/10.1002/joc.6517

Descamps, S., Aars, J., Fuglei, E., Kovacs, K. M., Lydersen, C., Pavlova, O., et al. (2017). Climate change impacts on wildlife in a High Arctic archipelago–Svalbard, Norway. *Global Change Biology*, *23*(2), 490–502. https://doi.org/10.1111/gcb.13381

Esau, I., & Repina, I. (2012). Wind climate in Kongsfjorden, Svalbard, and attribution of leading wind driving mechanisms through turbulence-resolving simulations. *Advances in Meteorology*, *2012*, 1–16. https://doi.org/10.1155/2012/568454

Førland, E., Benestad, R., Hanssen-Bauer, I., Haugen, J. E., & Skaugen, T. E. (2011). Temperature and precipitation development at Svalbard 1900–2100. In *Advances in meteorology, 2011*. Hindawi.

Førland, E., Hanssen-Bauer, I., & Nordli, O. (1997). *Climate statistics and long term series of temperature and precipitation at Svalbard and Jan Mayen, DNMI—Rapport, 21/97*. Norwegian Meteorological Institute.

Frank, L., Jonassen, M. O., Remes, T., Schalamon, F. R., & Stenlund, A. (2023). IWIN: The Isfjorden Weather Information Network. *Earth System Science Data*, *15*(9), 4219–4234. https://doi.org/10.5194/essd-15-4219-2023

Furevik, B. R., Johannessen, O. M., & Sandvik, A. D. (2002). SAR-retrieved wind in polar regions-Comparison with in situ data and atmospheric model output. *IEEE Transactions on Geoscience and Remote Sensing*, *40*(8), 1720–1732. https://doi.org/10.1109/tgrs.2002.802509

Gjelten, H. M., Nordli, O., Isaksen, K., Førland, E. J., Sviashchennikov, P. N., Wyszynski, P., et al. (2016). Air temperature variations and gradients along the coast and fjords of western Spitsbergen. *Polar Research*, *35*(1), 29878. https://doi.org/10.3402/polar.v35.29878

Haiden, T., Sandu, I., Balsamo, G., Arduini, G., & Beljaars, A. (2018). Addressing biases in near-surface forecasts. *ECMWF Newsletter*, *157*, 20–25.

Hanssen-Bauer, I., Førland, E., Hisdal, H., Mayer, S., Sandø, A., & Sorteberg, A. (2019). Climate in Svalbard 2100. A knowledge base for climate adaptation.

Hersbach, H., Bell, B., Berrisford, P., Hirahara, S., Horányi, A., Muñoz-Sabater, J., et al. (2020). The ERA5 global reanalysis. *Quarterly Journal of the Royal Meteorological Society*, *146*(730), 1999–2049. https://doi.org/10.1002/qj.3803

Hersbach, H., Bell, B., Berrisford, P., Hirahara, S., Horányi, A., Muñoz-Sabater, J., et al. (2018). ERA5 hourly data on single levels from 1959 to present [Dataset]. Copernicus Climate Change Service (C3S) Climate Data Store (CDS). https://doi.org/10.24381/cds.adbb2d47

Isaksen, K., Nordli, O., Førland, E. J., Lupikasza, E., Eastwood, S., & Niedźwiedź, T. (2016). Recent warming on Spitsbergen—Influence of atmospheric circulation and sea ice cover. *Journal of Geophysical Research: Atmospheres*, *121*(20), 11–913. https://doi.org/10.1002/2016jd025606

Isaksen, K., Nordli, O., Ivanov, B., Køltzow, M., Aaboe, S., Gjelten, H. M., et al. (2022). Exceptional warming over the Barents area. *Scientific Reports*, *12*(1), 1–18. https://doi.org/10.1038/s41598-022-13568-5

Jackson, P. L., & Steyn, D. G. (1994). Gap winds in a fjord. Part II: Hydraulic analog. *Monthly Weather Review*, *122*(12), 2666–2676. https://doi.org/10.1175/1520-0493(1994)122<2666:gwiafp>2.0.co;2

Køltzow, M., Casati, B., Bazile, E., Haiden, T., & Valkonen, T. (2019). An NWP model intercomparison of surface weather parameters in the European Arctic during the year of polar prediction special observing period Northern Hemisphere 1. *Weather and Forecasting*, *34*(4), 959–983. https://doi.org/10.1175/waf-d-19-0003.1

Køltzow, M., Schyberg, H., Støylen, E., & Yang, X. (2022). Value of the Copernicus Arctic Regional Reanalysis (CARRA) in representing near-surface temperature and wind speed in the north-east European Arctic. *Polar Research*, *41*. https://doi.org/10.33265/polar.v41.8002

Kossmann, M., & Sturman, A. P. (2003). Pressure-driven channeling effects in bent valleys. *Journal of Applied Meteorology and Climatology*, *42*(1), 151–158. https://doi.org/10.1175/1520-0450(2003)042<0151:pdceib>2.0.co;2

Kuttler, W., Weber, S., Schonnefeld, J., & Hesselschwerdt, A. (2007). Urban/rural atmospheric water vapour pressure differences and urban moisture excess in Krefeld, Germany. *International Journal of Climatology: A Journal of the Royal Meteorological Society*, *27*(14), 2005–2015. https://doi.org/10.1002/joc.1558

Li, C.-L., Bye, J. A., Gallagher, S. J., & Cowan, T. (2013). Annual sea surface temperature lag as an indicator of regional climate variability. *International Journal of Climatology*, *33*(10), 2309–2317. https://doi.org/10.1002/joc.3587

Lokoshchenko, M. A. (2017). Urban heat island and urban dry island in Moscow and their centennial changes. *Journal of Applied Meteorology and Climatology*, *56*(10), 2729–2745. https://doi.org/10.1175/jamc-d-16-0383.1

Moore, G., & Imrit, A. (2022). Impact of resolution on the representation of the mean and extreme winds along Nares Strait. *Journal of Geophysical Research: Atmospheres*, *127*(19), e2022JD037443. https://doi.org/10.1029/2022jd037443

Muckenhuber, S., Nilsen, F., Korosov, A., & Sandven, S. (2016). Sea ice cover in Isfjorden and Hornsund, Svalbard (2000-2014) from remote sensing data. *The Cryosphere*, *10*(1), 149–158. https://doi.org/10.5194/tc-10-149-2016

Müller, M., Batrak, Y., Kristiansen, J., Køltzow, M., Noer, G., & Korosov, A. (2017). Characteristics of a convective-scale weather forecasting system for the European Arctic. *Monthly Weather Review*, *145*(12), 4771–4787. https://doi.org/10.1175/mwr-d-17-0194.1

Nilsen, F., Cottier, F., Skogseth, R., & Mattsson, S. (2008). Fjord-shelf exchanges controlled by ice and brine production: The interannual variation of Atlantic Water in Isfjorden, Svalbard. *Continental Shelf Research*, *28*(14), 1838–1853. https://doi.org/10.1016/j.csr.2008.04.015

Nilsen, F., Skogseth, R., Vaardal-Lunde, J., & Inall, M. (2016). A simple shelf circulation model: Intrusion of Atlantic water on the West Spitsbergen Shelf. *Journal of Physical Oceanography*, *46*(4), 1209–1230. https://doi.org/10.1175/JPO-D-15-0058.1

Nordli, O., Przybylak, R., Ogilvie, A. E. J., & Isaksen, K. (2014). Long-term temperature trends and variability on Spitsbergen: The extended Svalbard Airport temperature series, 1898-2012. Polar research. https://doi.org/10.3402/polar.v33.21349

Onarheim, I. H., Smedsrud, L. H., Ingvaldsen, R. B., & Nilsen, F. (2014). Loss of sea ice during winter north of Svalbard. *Tellus A: Dynamic Meteorology and Oceanography*, *66*(1), 23933. https://doi.org/10.3402/tellusa.v66.23933

Peeters, B., Pedersen, A. O., Loe, L. E., Isaksen, K., Veiberg, V., Stien, A., et al. (2019). Spatiotemporal patterns of rain-on-snow and basal ice in high Arctic Svalbard: Detection of a climate-cryosphere regime shift. *Environmental Research Letters*, *14*(1), 015002. https://doi.org/10.1088/1748-9326/aaefb3

Prescott, J., & Collins, J. A. (1951). The lag of temperature behind solar radiation. *Quarterly Journal of the Royal Meteorological Society*, *77*(331), 121–126. https://doi.org/10.1002/qj.49707733112

Rantanen, M., Karpechko, A. Y., Lipponen, A., Nordling, K., Hyvärinen, O., Ruosteenoja, K., et al. (2022). The Arctic has warmed nearly four times faster than the globe since 1979. *Communications Earth & Environment*, *3*(1), 1–10. https://doi.org/10.1038/s43247-022-00498-3

Reeve, M. A., & Kolstad, E. W. (2011). The Spitsbergen South Cape tip jet. *Quarterly Journal of the Royal Meteorological Society*, *137*(660), 1739–1748. https://doi.org/10.1002/qj.876

Richards, K. (2005). Urban and rural dewfall, surface moisture, and associated canopy-level air temperature and humidity measurements for Vancouver, Canada. *Boundary-Layer Meteorology*, *114*(1), 143–163. https://doi.org/10.1007/s10546-004-8947-7

Sandvik, A. D., & Furevik, B. R. (2002). Case study of a coastal jet at Spitsbergen—Comparison of SAR-and model-estimated wind. *Monthly Weather Review*, *130*(4), 1040–1051. https://doi.org/10.1175/1520-0493(2002)130<1040:csoacj>2.0.co;2

Schuler, T. V., Kohler, J., Elagina, N., Hagen, J. O. M., Hodson, A. J., Jania, J. A., et al. (2020). Reconciling Svalbard glacier mass balance. *Frontiers in Earth Science*, *8*, 156. https://doi.org/10.3389/feart.2020.00156

Schyberg, H., Yang, X., Køltzow, M., Amstrup, B., Bakketun, A., Bazile, E., et al. (2020a). Arctic regional reanalysis on pressure levels from 1991 to present [Dataset]. Copernicus Climate Change Service (C3S) Climate Data Store (CDS). https://doi.org/10.24381/cds.e3c841ad

Schyberg, H., Yang, X., Køltzow, M., Amstrup, B., Bakketun, A., Bazile, E., et al. (2020b). Arctic regional reanalysis on single levels from 1991 to present [Dataset]. Copernicus Climate Change Service (C3S) Climate Data Store (CDS). https://doi.org/10.24381/cds.713858f6

Screen, J. A., & Simmonds, I. (2013). Exploring links between Arctic amplification and mid-latitude weather. *Geophysical Research Letters*, *40*(5), 959–964. https://doi.org/10.1002/grl.50174

Serreze, M. C., & Barry, R. G. (2011). Processes and impacts of Arctic amplification: A research synthesis. *Global and Planetary Change*, *77*(1–2), 85–96. https://doi.org/10.1016/j.gloplacha.2011.03.004

Skeie, P., & Gronas, S. (2000). Strongly stratified easterly flows across Spitsbergen. *Tellus, Series A: Dynamic Meteorology and Oceanography*, *52*(5), 473–486. https://doi.org/10.3402/tellusa.v52i5.12281

Skogseth, R., Olivier, L. L. A., Nilsen, F., Falck, E., Fraser, N., Tverberg, V., et al. (2020). Variability and decadal trends in the Isfjorden (Svalbard) ocean climate and circulation – An indicator for climate change in the European Arctic. *Progress in Oceanography*, *187*, 102394. https://doi.org/10.1016/j.pocean.2020.102394

Smedsrud, L. H., Esau, I., Ingvaldsen, R. B., Eldevik, T., Haugan, P. M., Li, C., et al. (2013). The role of the Barents Sea in the Arctic climate system. *Reviews of Geophysics*, *51*(3), 415–449. https://doi.org/10.1002/rog.20017

Smedsrud, L. H., Ingvaldsen, R., Nilsen, J. E., & Skagseth, O. (2010). Heat in the Barents Sea: Transport, storage, and surface fluxes. *Ocean Science*, *6*(1), 219–234. https://doi.org/10.5194/os-6-219-2010

Smith, D. M., Screen, J. A., Deser, C., Cohen, J., Fyfe, J. C., García-Serrano, J., et al. (2019). The polar amplification model intercomparison project (PAMIP) contribution to CMIP6: Investigating the causes and consequences of polar amplification. *Geoscientific Model Development*, *12*(3), 1139–1164. https://doi.org/10.5194/gmd-12-1139-2019

Tverberg, V., Skogseth, R., Cottier, F., Sundfjord, A., Walczowski, W., Inall, M. E., et al. (2019). The Kongsfjorden transect: Seasonal and inter-annual variability in hydrography. In *The ecosystem of Kongsfjorden, Svalbard* (pp. 49–104). Springer.

Valkonen, T., Stoll, P., Batrak, Y., Køltzow, M., Schneider, T. M., Stigter, E. E., et al. (2020). Evaluation of a sub-kilometre NWP system in an Arctic fjord-valley system in winter. *Tellus A: Dynamic Meteorology and Oceanography*, *72*(1), 1–21. https://doi.org/10.1080/16000870.2020.1838181

Vihma, T. (2014). Effects of Arctic sea ice decline on weather and climate: A review. *Surveys in Geophysics*, *35*(5), 1175–1214. https://doi.org/10.1007/s10712-014-9284-0

Vihma, T., Kilpeläinen, T., Manninen, M., Sjöblom, A., Jakobson, E., Palo, T., et al. (2011). Characteristics of temperature and humidity inversions and low-level jets over Svalbard fjords in spring. *Advances in Meteorology*, *2011*, 1–14. https://doi.org/10.1155/2011/486807

Vihma, T., Pirazzini, R., Fer, I., Renfrew, I. A., Sedlar, J., Tjernström, M., et al. (2014). Advances in understanding and parameterization of small-scale physical processes in the marine Arctic climate system: A review. *Atmospheric Chemistry and Physics*, *14*(17), 9403–9450. https://doi.org/10.5194/acp-14-9403-2014

Vihtakari, M., Sundfjord, A., & de Steur, L. (2019). *Barents sea ocean-current*. Norwegian Polar Institute and Institute of Marine Research. Retrieved from https://github.com/MikkoVihtakari/Barents-Sea-currents

Walczowski, W., & Piechura, J. (2011). Influence of the West Spitsbergen Current on the local climate. *International Journal of Climatology*, *31*(7), 1088–1093. https://doi.org/10.1002/joc.2338

Wang, Z., Song, J., Chan, P. W., & Li, Y. (2021). The urban moisture island phenomenon and its mechanisms in a high-rise high-density city. *International Journal of Climatology*, *41*(S1), E150–E170. https://doi.org/10.1002/joc.6672

Whiteman, C. D., & Doran, C. (1993). The relationship between overlying synoptic-scale flows and winds within a valley. *Journal of Applied Meteorology and Climatology*, *32*(11), 1669–1682. https://doi.org/10.1175/1520-0450(1993)032<1669:trboss>2.0.co;2

Wickström, S., Jonassen, M., Cassano, J., & Vihma, T. (2020). Present temperature, precipitation, and rain-on-snow climate in Svalbard. *Journal of Geophysical Research: Atmospheres*, *125*(14), e2019JD032155. https://doi.org/10.1029/2019JD032155

Wickström, S., Jonassen, M., Vihma, T., & Uotila, P. (2020). Trends in cyclones in the high-latitude North Atlantic during 1979–2016. *Quarterly Journal of the Royal Meteorological Society*, *146*(727), 762–779. https://doi.org/10.1002/qj.3707

Yang, X., Nielsen, K. P., Amstrup, B., Peralta, C., Høyer, J., Englyst, P. N., et al. (2020). *C3S Arctic regional reanalysis – Full system documentation*. Copernicus Climate Change Service. Retrieved from https://datastore.copernicus-climate.eu/documents/reanalysis-carra/CARRAFull-SystemDocumentationFinal.pdf

Zahn, M., Akperov, M., Rinke, A., Feser, F., & Mokhov, I. I. (2018). Trends of cyclone characteristics in the Arctic and their patterns from different reanalysis data. *Journal of Geophysical Research: Atmospheres*, *123*(5), 2737–2751. https://doi.org/10.1002/2017jd027439

Zilitinkevich, S. S., & Esau, I. N. (2005). Resistance and heat-transfer laws for stable and neutral planetary boundary layers: Old theory advanced and re-evaluated. *Quarterly Journal of the Royal Meteorological Society: A journal of the atmospheric sciences, applied meteorology and physical oceanography*, *131*(609), 1863–1892. https://doi.org/10.1256/qj.04.143

References From the Supporting Information

Donlon, C. J., Martin, M., Stark, J., Roberts-Jones, J., Fiedler, E., & Wimmer, W. (2012). The operational sea surface temperature and sea ice analysis (OSTIA) system. *Remote Sensing of Environment*, *116*, 140–158. https://doi.org/10.1016/j.rse.2010.10.017

Jakobsson, M., Mayer, L. A., Bringensparr, C., Castro, C. F., Mohammad, R., Johnson, P., et al. (2020). The international bathymetric chart of the Arctic Ocean version 4.0. *Scientific Data*, *7*(1), 176. https://doi.org/10.1038/s41597-020-0520-9

Merchant, C., Embury, O., Roberts-Jones, J., Fiedler, E., Bulgin, C., Corlett, G., et al. (2016). *ESA sea surface temperature climate change initiative (ESA SST CCI): Analysis long term product version 1.1*. NERC Earth Observation Data Centre.

Pedersen, L., Dybkjær, G., Eastwood, S., Heygster, G., Ivanova, N., Kern, S., et al. (2017). *Sea ice concentration climate data record from the AMSR-E and AMSR-2 instruments at 25km grid spacing, version 2.1*. Centre for Environmental Data Analysis.

Tonboe, R. T., Eastwood, S., Lavergne, T., Sørensen, A. M., Rathmann, N., Dybkjær, G., et al. (2016). The EUMETSAT sea ice concentration climate data record. *The Cryosphere*, *10*(5), 2275–2290. https://doi.org/10.5194/tc-10-2275-2016